Journal of Solid State Chemistry **149,** 360–369 (2000)
doi:10.1006/jssc.1999.8546, available online at http://www.idealibrary.com on IDEAL®

A-Site Cation-Vacancy Ordering in $Sr_{1-3x/2}La_xTiO_3$: A Study by HRTEM

P. D. Battle,*,[1] J. E. Bennett,* J. Sloan,* R. J. D. Tilley,† and J. F. Vente*

*Inorganic Chemistry Laboratory, Oxford University, South Parks Road, Oxford, OX1 3QR, United Kingdom; and †School of Engineering, University of Wales, Cardiff, P.O. Box 917, Cardiff, CF2 1XH, United Kingdom

Received August 13, 1999; in revised form October 5, 1999; accepted October 22, 1999

The system $Sr_{1-3x/2}La_xTiO_3$ ($0.25 \leq x \leq 0.6$) has been studied by high-resolution transmission electron microscopy, allowing the direct observation of vacant sites on the Sr/La sublattice of the perovskite structure. Isolated vacancies are observed in 2D structural projections of samples having $x \sim 0.3$. Vacancy pairing occurs with increasing La concentration, followed by the formation of vacancy squares of side $2a_0$ and vacancy rectangles $2a_0 \times a_0$. The latter signify vacancy ordering in an orthorhombic superstructure, and the former are considered to derive from orthogonal superstructure microdomains. The details of the ordering are sensitive to the heat treatment used during preparation of the sample.

INTRODUCTION

The perovskite structure has been central to many of the recent developments in solid state chemistry, including high-temperature superconductivity and colossal magnetoresistance. Progress in these research areas has relied on the ability of the ABO_3 structure type to accommodate a wide range of chemical substitutions over both the A site (ideally 12 coordinate) and the B site (ideally 6 coordinate). The 1:1 substitution of trivalent cations onto an A sublattice occupied by divalent cations is usually charge-compensated by the reduction of a transition metal cation on the B site. Alternatively, the introduction of A'^{3+} into a compound $A^{2+}BO_3$ can be accommodated by the introduction of vacancies on the A sublattice; that is, the substitution ratio is 2:3 rather than 1:1. Previous work (1) has demonstrated that the system $Sr_{1-3x/2}La_xTiO_3$ ($0 \leq x \leq \frac{2}{3}$) shows the latter type of behavior, with $SrTiO_3$ and $La_{2/3}TiO_3$(2) as the limiting compositions. For low levels of substitution the A-site vacancies are expected to be distributed randomly through the crystal structure, but ordering is likely to occur when the concentration exceeds a critical value which is itself temperature dependent. Tien and Hummel (1) observed that furnace-cooled samples of $Sr_{1-3x/2}La_xTiO_3$ prepared at 1400°C had a simple cubic perovskite structure when $x < 0.467$, whereas the X-ray diffraction patterns of samples having $x \geq 0.467$ showed superlattice lines consistent with a doubling of the cubic unit cell parameter; the superlattice lines were absent when the samples were cooled by air-quenching. Bouwma *et al.* (3) obtained similar results for a furnace-cooled sample with $x = 0.5$, although they interpreted their data in terms of a tetragonal unit cell similar to that used by Abe and Uchino (2) to describe the $x = \frac{2}{3}$ end member, $La_{2/3}TiO_3$. Other groups have subsequently studied this system and there is general agreement that $x = 0.5$ can be prepared with a noncubic superstructure although Shoup *et al.* (4) found no correlation between the rate of cooling and the formation of the ordered phase. However, it is worth noting that Balachandran and Eror (5) observed a pyrochlore phase in compositions with $x \geq 0.4$ and that they did not see any evidence of an ordered perovskite phase.

The investigations described above have used X-ray powder diffraction as their principal structural probe. A number of ordered defect structures have been proposed in order to account for the transition from cubic to tetragonal symmetry, but none of them has been fully consistent with the diffraction data. We describe below a study of both air-quenched and furnace-cooled samples of $Sr_{1-3x/2}La_xTiO_3$ ($0.25 \leq x \leq 0.6$) in which high-resolution transmission electron microscopy (HRTEM) and electron diffraction (ED) have been used to probe the details of the defect structure.

EXPERIMENTAL

The synthesis of our samples was carried out in two stages. First the compound was synthesized as a pure perovskite phase; then aliquots of the product were subjected to different heat treatments (furnace cooling or air quenching). The pure compounds were synthesized using the standard ceramic method. Intimately mixed stoichiometric quantities of dried La_2O_3, $SrCO_3$, and TiO_2 (all of purity $>99.99\%$) were prefired at 800°C to remove CO_2 and then pelletized and heated in air for one day at 1000°C. They were then heated in air at 1200°C for a minimum of four days and

[1]To whom correspondence should be addressed.

0022-4596/00 $35.00

a maximum of seven days. In the case of the air-quenched samples, the final heat treatment involved heating a ~ 1 g portion in air at 1400°C for four hours, allowing it to cool rapidly in the furnace to 1200°C, and then air quenching it to room temperature. A sample having $x = 0.5$ was also quenched into liquid nitrogen in order to establish the influence of different quenching rates. Furnace-cooled samples were prepared by heating the initial product at 1400°C for four hours and then cooling it to 500°C at a rate of 0.1°C min^{-1} before air quenching to room temperature. In the case of the composition $x = 0.5$, an extra specimen was prepared by cooling from 1400°C at 0.05°C min^{-1}. The reaction products were characterized at room temperature by X-ray powder diffraction (XRD), the data being collected in Bragg–Brentano geometry on a Siemens D5000 diffractometer using Cu$K\alpha_1$ radiation. The data, collected with a step size $\Delta 2\theta = 0.02°$ over the angular range $5 \leq 2\theta$ (°) ≤ 120, were analyzed using the version of the Rietveld method (6) implemented in the GSAS program package (7). The peak shape was described by a pseudo-Voigt function, and the background by a shifted Chebyshev function. Selected reaction products were also studied in a JEOL 4000EX high-resolution transmission electron microscope (HRTEM) operated at 400 kV ($C_s = 0.9$ nm; point resolution 1.6 Å) and equipped with a top-loading double-tilt goniometer specimen stage ($\pm 20°$). Lattice images were recorded at or near optimum Scherzer defocus conditions and compared to composite image simulations calculated using the "supercell" option in the Stadelmann EMS program (8). The supercells used in our calculations consisted of $(4 \times 4 \times 4)$ or $(4 \times 4 \times 8)$ arrays of cubic $SrTiO_3$ unit cells. In order to simulate the image contrast due to the vacancies, Sr atoms were removed from the appropriate sites, as described below. Fast Fourier transforms (FFTs) were calculated from selected regions of lattice images using the Digital Micrograph program (9). Measurements of magnetic susceptibility, performed on a Quantum Design MPMS SQUID magnetometer over the temperature range $5 < T$ (K) < 300, enabled us to calculate a typical spin concentration of $\sim 7 \times 10^{-3}$ per formula unit. This is a measure of the extent to which the Ti cations are fully oxidized.

RESULTS

a. X-Ray Studies of Furnace-Cooled Specimens

Furnace-cooled samples having La contents $x = 0.25$, 0.30, and 0.40 appeared monophasic, giving rise to XRD patterns which could be indexed in a primitive cubic unit cell with $a = 3.89617(2)$, 3.89395(8), and 3.88874(8) Å respectively. In each case a satisfactory ($\chi^2 < 1.4$) account of the observed intensity distribution was obtained in the space group ($Pm3m$) associated with the simple perovskite structure; there are no variable atomic coordinates in this model.

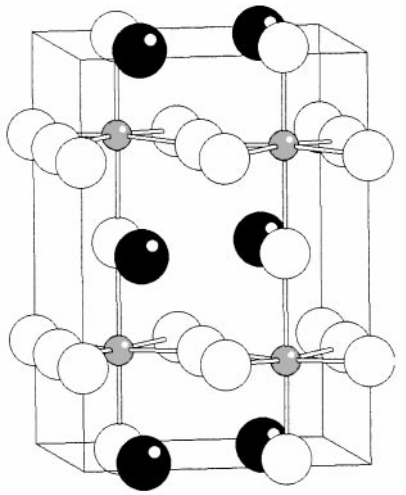

FIG. 1. Crystal structure of orthorhombic $Sr_{1-3x/2}La_xTiO_3$; black, white, and gray circles represent Sr/La, O, and Ti, respectively.

The X-ray data collected from the slow-cooled $x = 0.5$ samples contained weak peaks ($2\theta = 11.66$ and 25.74°) which could not be indexed on the unit cell described above. The relative intensities of these peaks were the same in the two aliquots cooled at different rates, and we report only the analysis of the data from the specimen cooled at the same rate (0.1°C min^{-1}) as the other compositions. The angular positions of the additional reflections were consistent with those reported previously (1, 3, 4, 10), but the intensity distribution was not consistent with the tetragonal description of $La_{2/3}TiO_3$ provided by Abe *et al.* (2). It was more compatible with that proposed recently by MacEachern *et al.* (11), and we were able to account for all the observed peaks using a structural model (Fig. 1) in the orthorhombic space group *Pban*. In common with the majority of the literature, our work thus contradicts previous claims (5, 12) that the composition $Sr_{0.25}La_{0.5}TiO_3$ is inaccessible as a single phase. The atomic coordinates which would be used to describe a perovskite of stoichiometry ABO_3 in this space group are listed in Table 1; the unit cell parameters are

TABLE 1
Atomic Coordinates for the Perovskite ABO_3 in Space Group *Pban*

Atom	Site	x	y	z
A(1)	2a	$\frac{1}{4}$	$\frac{1}{4}$	0
A(2)	2d	$\frac{1}{4}$	$\frac{1}{4}$	$\frac{1}{2}$
B	4l	$\frac{1}{4}$	$\frac{3}{4}$	z
O(1)	8m	x	y	z
O(2)	2c	$\frac{3}{4}$	$\frac{1}{4}$	$\frac{1}{2}$
O(3)	2b	$\frac{3}{4}$	$\frac{1}{4}$	0

Note. $z_B \sim 0.25$; $(x, y, z)_{O1} \sim 0.0, 0.0, 0.25$.

$a \sim \sqrt{2a_0}$, $b \sim \sqrt{2}a_0$, $c \sim 2a_0$, where $a_0 \sim 3.89$ Å, that is, the unit cell parameter of the primitive cubic perovskite structure. The presence of three species (La, Sr, and vacancies) on the two crystallographically distinct A sites means that least-squares Rietveld analysis cannot lead to a unique description of the structure unless constraints are applied. After a number of test calculations, we chose to assume that the La/Sr ratio on each A site was 2:1, as in the bulk sample. We thus excluded the possibility of La/Sr ordering in order to include (La, Sr)/vacancy ordering. The best agreement between the observed and calculated diffraction patterns ($\chi^2 = 1.34$) was then given by the parameters listed in Table 2. The weakly scattering anion O(1) was fixed at $(0, 0, \frac{1}{4})$ in all our refinements, and the thermal parameters of all atoms were set to zero. All the test models which gave comparable agreement had unequal fractional occupancies for the sites A(1) and A(2). Thus although we cannot claim that the tabulated parameters constitute a unique description of the structure, we are confident that this $x = 0.5$ sample shows a partial ordering of the cation vacancies over the two available A sites. The other noteworthy structural feature is the asymmetric Ti–O bonding parallel to z; the displacement of the cation away from $z = 0.25$ results in the Ti–O(2) bond (1.911 Å) being significantly shorter than the Ti–O(3) bond (1.973 Å). The XRD pattern of the slow-cooled $x = 0.6$ sample was more complex than those described above. The superlattice reflections observed for $x = 0.5$ were relatively strong and other peaks were split, indicating either a lowering of symmetry or the presence of more than one phase. We are unable to identify peaks corresponding to $La_2Ti_2O_7$, previously (5) found as an impurity in this system, and the XRD pattern remains unindexed.

b. X-Ray Studies of Air-Quenched Specimens

The XRD pattern of the air-quenched $x = 0.25$ sample revealed the presence of $\sim$10% TiO_2 in addition to a simple cubic perovskite having a unit cell parameter $a = 3.89466(4)$ Å. The behavior of this composition is still under investigation and will not be discussed further here.

TABLE 2
Structural Parameters for Furnace-Cooled $Sr_{0.25}La_{0.5}TiO_3$

Site	Site Occupancies		% vacancies
	% La	% Sr	
A(1)	56.6(2)	28.3	15.1
A(2)	43.4(2)	21.7	34.9

Note. Space group *Pban*, $a = 5.4937(2)$ Å, $b = 5.4964(2)$ Å, $c = 7.7676(3)$ Å, $V = 234.550(8)$ Å^3, $z_{Ti} = 0.246(1)$.

TABLE 3
Structural Parameters for Air-Quenched $Sr_{0.1}La_{0.6}TiO_3$

Site	Site Occupancies		% vacancies
	% La	% Sr	
A(1)	48.1(3)	8.0	43.9
A(2)	71.9(3)	12.0	16.1

Note. Space group *Pban*, $a = 5.4925(6)$ Å, $5.4937(6)$ Å, $c = 7.7562(2)$ Å, $V = 234.04$ Å^3, $z_{Ti} = 0.2386(9)$.

Samples having $x = 0.3$, 0.4, and 0.5 gave rise to XRD patterns which could be indexed in a primitive cubic unit cell with $a = 3.8945(1)$, 3.88932(9), and 3.88501(8) Å, respectively, whereas the presence of superlattice lines required the use of the orthorhombic space group *Pban* for $x = 0.6$; the superlattice lines were significantly stronger in this case than in that of the furnace-cooled $x = 0.5$ sample. Rietveld refinements (Table 3) provided evidence for vacancy ordering, but again the occupancy factors are not a unique description of the structure, merely an indication of ordering. Figure 2 contrasts the observed and calculated XRD patterns of $x = 0.3$ ($\chi^2 = 1.39$) and $x = 0.6$ ($\chi^2 = 1.30$) and shows the relative magnitude of the fundamental peaks and those due to the superlattice; the latter appear in Fig. 2b but not in Fig. 2a. The observed patterns from both samples contain a very weak peak at $2\theta \sim 30^\circ$, which presumably arises from a common, low-level impurity.

c. Electron Microscopy Studies

From the point of view of both electron diffraction (ED) and HRTEM lattice imaging, the most useful projection for studying the $Sr_{1-3x/2}La_xTiO_3$ series was the generalized [100] projection considered relative to a cubic ABO_3 parent as this gave the most readily interpretable information concerning both the cation/vacancy ordering behavior and the superstructure ordering that occurred increasingly as the composition approached $x = 0.6$. In the lattice images described below, vacancies can readily be distinguished from occupied A-cation sites (OS) by the appearance of white crosses in the image contrast, a consequence of the dark spot representing an occupied site being replaced by a white spot representing a vacancy. The pattern of vacancy formation in each of the specimens, particularly close to the crystal edges, provides a clear pattern of ordering as the overall composition approaches $x = 0.6$.

In Figs 3a–3d, the change in the [100] zone ED pattern for the furnace-cooled specimens as the composition is varied from $x = 0.3$ to $x = 0.6$ can clearly be seen. In Fig. 3a, corresponding to $x = 0.3$, a pattern closely resembling the [100] zone for phase-pure $SrTiO_3$ is observed. In Fig. 3b,

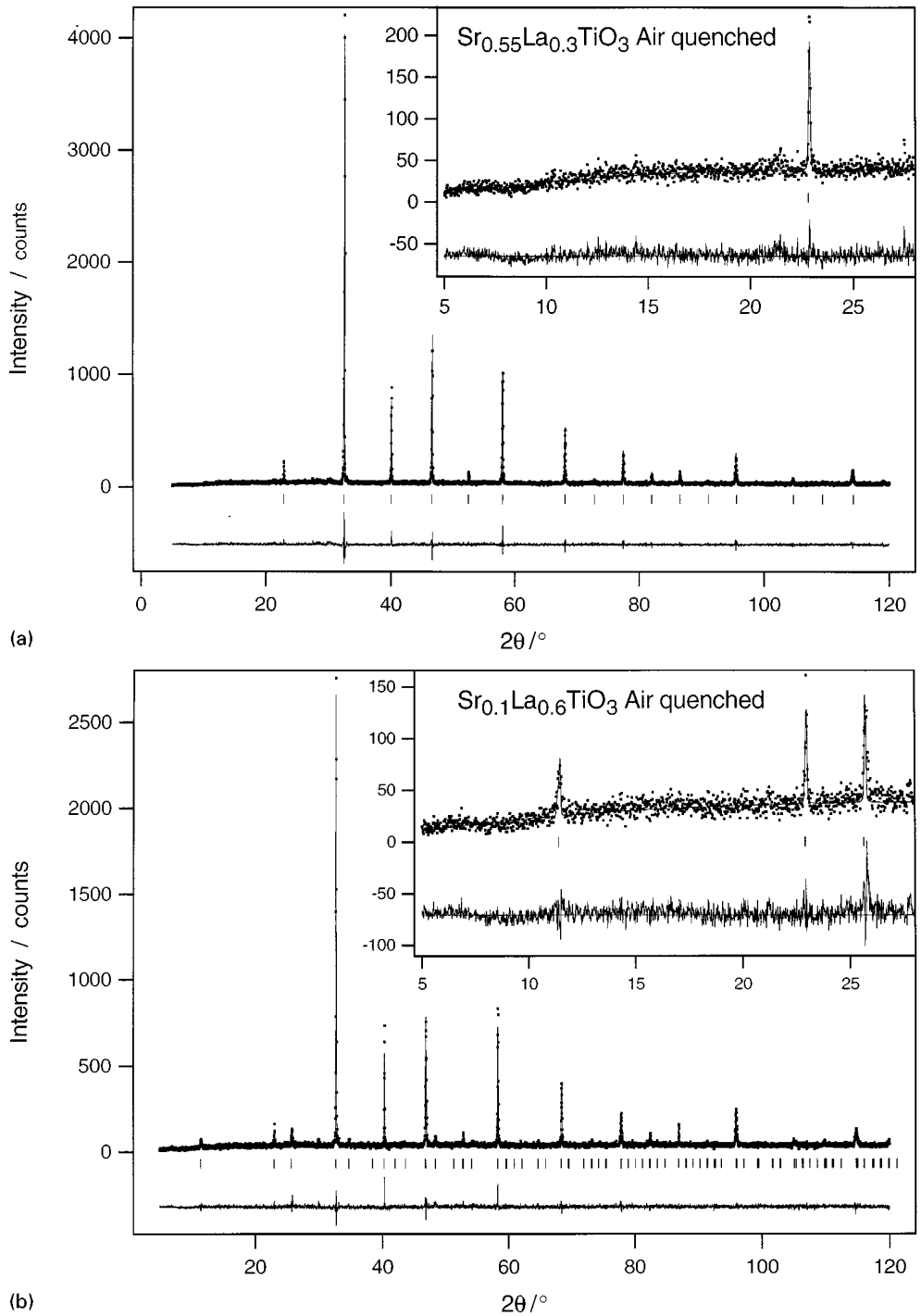

FIG. 2. Observed, calculated, and difference X-ray powder diffraction patterns of air-quenched $Sr_{1-3x/2}La_xTiO_3$ for (a) cubic $x = 0.3$ and (b) orthorhombic $x = 0.6$.

corresponding to $x = 0.4$, the same pattern is observed but diffuse reflections, labeled $(0\ \frac{1}{2}\ 0)$ and $(0\ 0\ \frac{1}{2})$, appear along both [010] and [001]. In the case of Fig. 3c, corresponding to $x = 0.5$, a further reflection is observed along [011], labeled $(0\ \frac{1}{2}\ \frac{1}{2})$. The diffraction pattern shown in Fig. 3d, corresponding to $x = 0.6$, can be indexed as the [110] zone of an orthorhombic phase, and the indices have been changed accordingly. It is significant that some of the

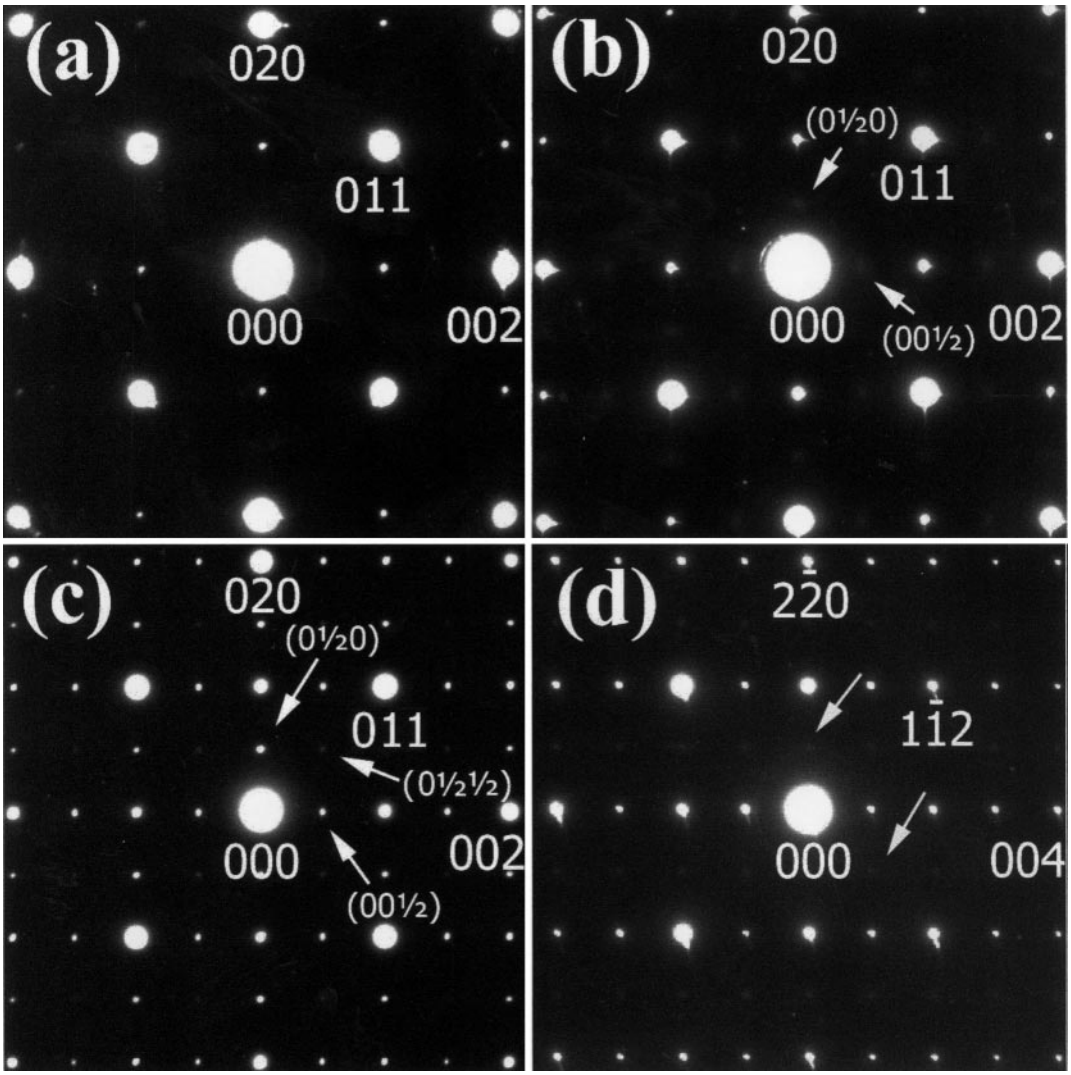

FIG. 3. Electron diffraction patterns of furnace-cooled $Sr_{1-3x/2}La_x\ TiO_3$ indexed for (a) $x = 0.3$, (b) $x = 0.4$, and (c) $x = 0.5$ as the [100] zone of a cubic system; (d) $x = 0.6$ is indexed as the [110] zone of an orthorhombic system. Arrows indicate weak reflections.

reflections which appeared in Fig. 3c are absent from Fig. 3d. Specifically, the half-integer superlattice reflections observed along both [010] and [001] in Fig. 3c are only seen along one axis, [001], in Fig. 3d. The only additional reflections observed along $[1\bar{1}0]$ of this pattern are diffuse and weak, possibly corresponding to a twinned domain of the same structure.

In Figs. 4a–4d, the microstructures which produce the ED patterns in Fig. 3 can be seen, and they clearly show the relationship between vacancy ordering and composition. Figure 4a shows the microstructure of the $x = 0.3$ composition; only a few dispersed *A*-site vacancies, appearing as white crosses, are apparent in the lattice image. Occasionally these are visible as pairs (bracketed) within the crystal. In Fig. 4b ($x = 0.4$), vacancy pairs (brackets + arrows) and discrete vacancies (arrows only) are visible in greater concentration throughout the crystal. It is noteworthy that vacancies may form on adjacent sites (Fig. 4a) or on alternate sites (Fig. 4b). In Fig. 4c ($x = 0.5$), vacancies form in small domains consisting of "squares" of dimension $2a_0 \times 2a_0$ in which the vacancies are on alternate *A* sites along each of two perpendicular axes. Alternatively the vacancies form "rectangles" ($2a_0 \times a_0$) in which the vacancies are on successive sites along the shorter side and alternate sites along the longer side. In Fig. 4d, the relative concentration of the rectangles increases, particularly near the edge of the crystal, and the ordering giving rise to the overall orthorhombic crystal symmetry becomes apparent.

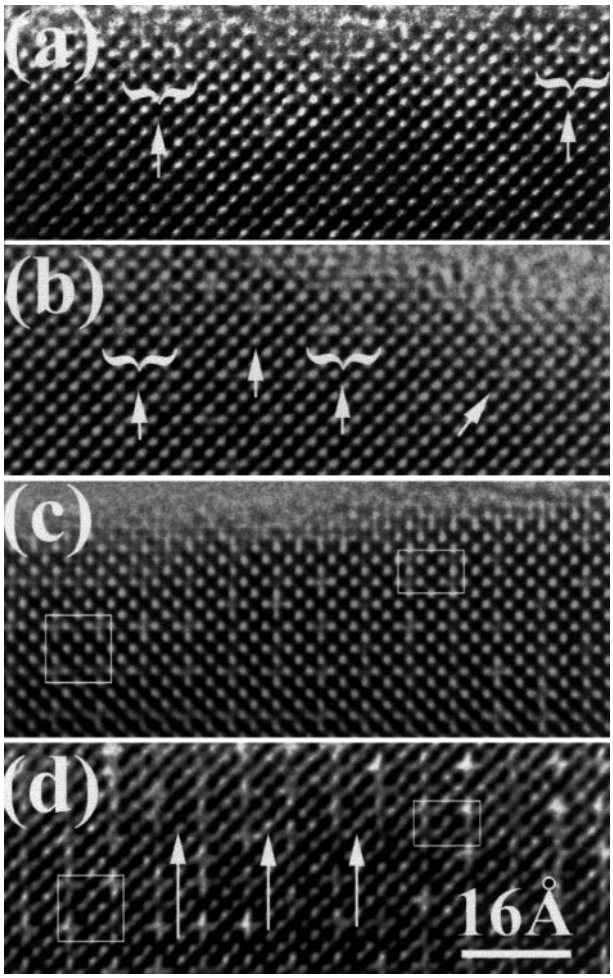

FIG. 4. Lattice images of furnace-cooled $Sr_{1-3x/2}La_xTiO_3$ projected along [100] of a cubic system for (a) $x = 0.3$, (b) $x = 0.4$, (c) $x = 0.5$, and along [110] of an orthorhombic system for (d) $x = 0.6$. The arrows in (a) and (b) point to isolated vacancies or vacancy pairs (bracketed). Square and rectangular vacancy groups are indicated in (c) and (d), and the arrows in (d) indicate the $[1\bar{1}0]$ direction.

In Fig. 5, the influence of cooling regime on crystalline order in the $x = 0.5$ composition can be seen. Figure 5a corresponds to air-quenched $x = 0.5$. In this case, the blurring of the superstructure reflections along [010] and [001] can clearly be seen. In the specimen cooled at $0.1°C\ min^{-1}$ (Fig. 5b), the diffuse reflections are much sharper and weak additional reflections along [011] are just visible. In Fig. 5c, taken from the sample that was cooled slowly over two weeks, the additional reflections along [011] are much stronger. In Figs. 6a–6c, the corresponding effects on crystalline ordering can be seen. In Fig. 6a, vacancies and vacancy pairs are randomly dispersed throughout the crystal. In Fig. 6b and 6c a far greater degree of ordering is observed. However, even in the crystal cooled for two weeks (Fig. 6c), ordering is not complete in the [100] zone and the square vacancy groups are interspersed with occupied *A* sites (OS). The sensitivity of the diffraction pattern to the vacancy concentration and ordering can be seen by considering the diffraction patterns calculated in Fig. 7 by taking the Fourier transform of two different regions, *A* and *B*, of the same crystallite of slow-cooled $Sr_{0.25}La_{0.5}TiO_3$. Region *A* leads to a diffraction pattern characteristic of a unit cell twice as large as that generated by region B.

The faint appearance of the central spot in some of the white crosses in region *A* of Fig. 7 suggests that vacancy ordering is also incomplete parallel to the projection axis. The simulated images shown in Fig. 8 can be used to gauge qualitatively the extent of vacancy ordering parallel to the projection axis. The simulations in Figs. 8a–8d were obtained from a $(4 \times 4 \times 4)$ supercell from which *A*-site cations had been removed in a systematic manner. For each of the simulations (4×4) cells are visible in the plane of the page, and the supercell is four layers thick (ca. 15 Å) in projection (i.e., effectively beneath the plane of the page). Figure 8a shows simulated images at 50-Å defocus intervals for the case where no vacancies have been created in the four-layer supercell. In the defocus range from -370 to -470 Å (i.e., just above and at Scherzer defocus, respectively, for the 4000EX), the dark spots correspond to the cation positions in the $(4 \times 4 \times 4)$ $SrTiO_3$ cell. Below the Scherzer defocus (-520 to -570 Å), the contrast corresponding to the cation positions reverses and they appear as white spots. In Fig. 8b four cations have been removed from alternating sites in the top surface of the crystal only. The columns of Sr cations containing these unoccupied sites appear with increasingly reduced contrast on moving from -370 to -520 Å and as complex white crosses at -570 Å defocus. In Fig. 8c, alternating *A*-site cation positions have been emptied in the two uppermost layers. Now the columns with unoccupied sites appear as strong white crosses at and below Scherzer defocus and with somewhat reduced contrast above Scherzer defocus. In Fig. 8d, four cations have been removed from corresponding sites on alternating layers, and the contrast is similar to that in 8c. Figs. 8e and 8f represent thicker crystals, $(4 \times 4 \times 8)$, with the former having the same vacancy concentration as Fig. 8b and the latter having the same as Fig. 8d. The conditions used in the collection of our experimental data are best approximated by the simulations at -420 and -470 Å. Our simulations show that for a given crystal thickness, the image contrast is a function only of vacancy concentration and not of vacancy disposition. The contrast variations become more obvious with increasing crystal thickness. In general, at Scherzer defocus, our observed images resemble Fig. 8f most closely. We conclude that in our samples there is usually an occupation factor of $\sim 50\%$ along the vacancy columns parallel to the axis of projection. However, this is only an estimate of the typical value, and it is clear from the contrast variations in the micrographs that some columns contain a lower vacancy

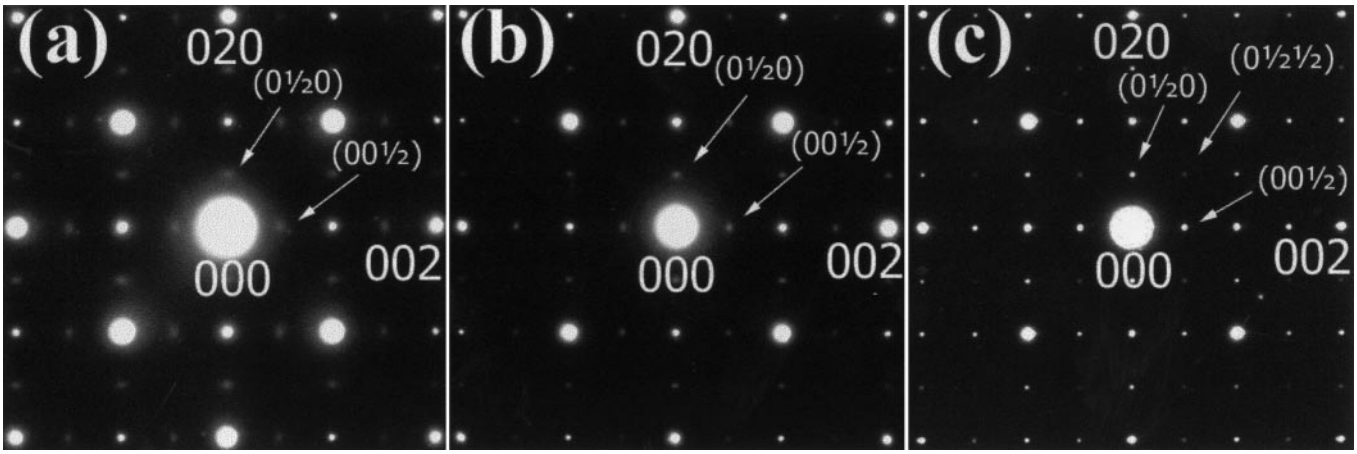

FIG. 5. The [100] electron diffraction patterns of $Sr_{0.25}La_{0.5}TiO_3$ samples which were (a) air-quenched, (b) cooled at $0.1^{\circ}C\ min^{-1}$, and (c) cooled at $0.05^{\circ}C\ min^{-1}$.

concentration. A direct comparison of the simulated and observed image contrasts is provided by Figs. 9a and 9b.

DISCUSSION

The results of this work confirm much of what has been written about this system previously, but, more importantly, they give insight into the changes in microstructure which accompany the changes in the crystal structure of the bulk. The XRD studies suggest that compounds with a low concentration of La have cubic symmetry, consistent with a random arrangement of vacancies; the La concentration needed to induce vacancy ordering is a function of the preparative method. This is not a new conclusion, although the majority of the previous studies, the exception being that by MacEachern *et al.* (11), have considered the superlattice to be tetragonal rather than orthorhombic. The displacement of the Ti cation (away from the centre of the TiO_6 coordination octahedron) which occurs in the orthorhombic structure has been seen in many ferroelectric titanates, but in this case it results in a sequence of long–short–short–long Ti–O bond lengths along the z axis of the orthorhombic unit cell; there is thus no net polarization. The structure contains two crystallographically independent sets of Sr/La sites, those at $z = 0$ and those at $z = 0.5$. The cation/vacancy ordering thus occurs along z and creates alternately cation-rich and vacancy-rich xy sheets, the separation between pairs of vacancy-rich sheets being $2a_0$. The space group *Pban* does not allow cation/vacancy ordering within the xy planes at $z = 0$ or $z = 0.5$.

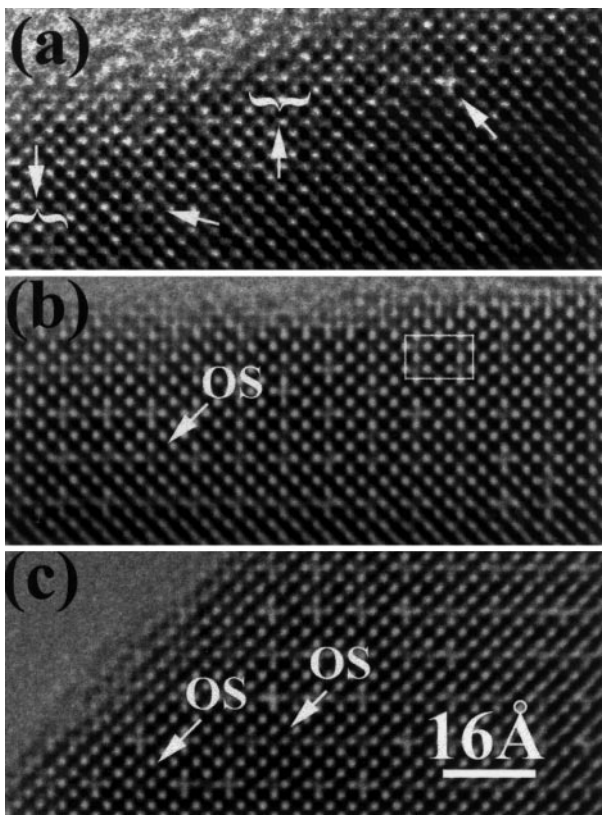

FIG. 6. The [100] lattice images of $Sr_{0.25}La_{0.5}TiO_3$ samples which were (a) air-quenched, (b) cooled at $0.1^{\circ}C\ min^{-1}$, and (c) cooled at $0.05^{\circ}C\ min^{-1}$. Occupied A sites which break the vacancy ordering are marked OS.

Comparison of the XRD and ED data for the furnace-cooled samples enphasizes the different sensitivities of the two techniques and the complexities of the system; ED effectively selects a single crystal from a polycrystalline sample, whereas XRD looks at the bulk sample. Both radiations lead to the $x = 0.30$ sample being described as primitive cubic. However, for $x = 0.40$ diffuse superlattice reflections indicative of cell doubling are observed in the ED data, whereas the XRD data can still be indexed in a primitive cubic unit cell. This implies that, at $x = 0.4$, the superstructure is only coherent over relatively short distances. On increasing the La concentration to $x = 0.5$, the [100] ED pattern from the selected crystal can apparently be indexed in a doubled cubic cell (i.e., $a = 2a_0$), but Rietveld profile

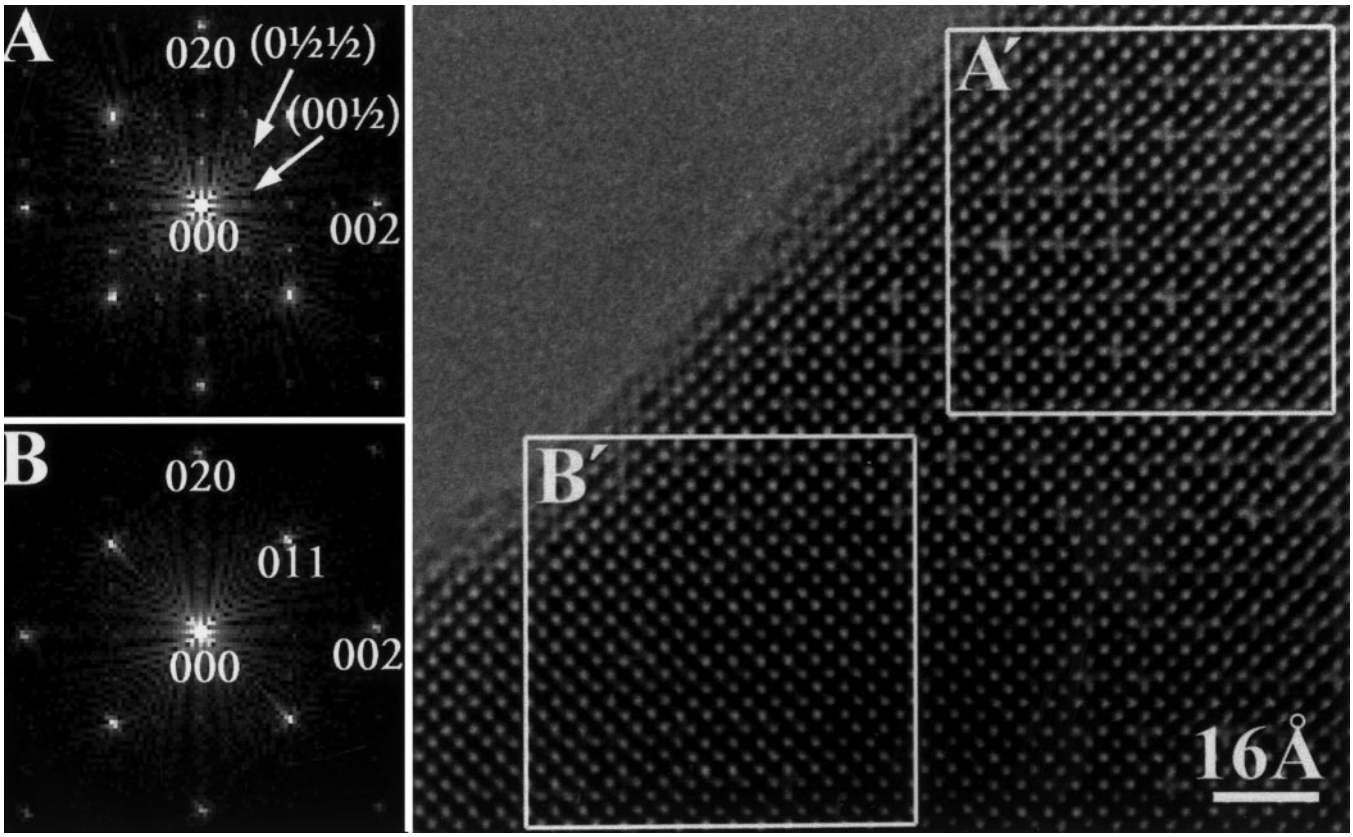

FIG. 7. The [100] ED patterns (*A* and *B*) generated by taking the Fourier transform of circular regions within the squares labeled *A′* and *B′* on the lattice image of a crystallite (see Fig. 6c) of slow-cooled $Sr_{0.25}La_{0.5}TiO_3$.

analysis of the XRD pattern suggests that the symmetry is orthorhombic. This can be explained if we assume that the ED pattern in Fig. 3c comes from a crystallite containing orthogonal orthorhombic microdomains, each of which has an ED pattern similar to that shown for $x = 0.6$ in Fig. 3d. This is consistent with the interpretation of the lattice image which we offer below. The XRD pattern (not shown) of the $x = 0.60$ furnace-cooled sample was complex, suggesting that a second phase is present. However, ED showed that an ordered orthorhombic phase is amongst those present.

The lattice images in Fig. 4 show that the changes in the diffraction pattern are the result of vacancy ordering on the *A* sublattice. As the La concentration increases, the vacancies begin to pair up and then to form $2a_0 \times 2a_0$ squares or $2a_0 \times a_0$ rectangles (Fig. 4c). The rectangles, where the $2a_0$ repeat distance only occurs in one direction, are units in a well-ordered orthorhombic region. In Fig. 4d, for $x = 0.6$, a well-developed ordering with a periodicity of $2a_0$ in a direction perpendicular to the arrows can be seen, whereas the distribution of vacancies parallel to the arrows is random, with separations of both a_0 and $2a_0$ occuring; the direction perpendicular to the arrows can thus be identified as the *z* axis of the orthorhombic unit cell. The formation of squares, that is, the vacancy ordering in two directions, is inconsistent with space group *Pban* and can be thought of as the growth of orthorhombic microdomains with mutually perpendicular *z* axes; these regions appear cubic in diffraction patterns. The diffraction pattern in Fig. 3c can thus be thought of as the superposition of two orthorhombic patterns similar to Fig. 3d, one rotated by 90° with respect to the other. This is consistent with the loss of superlattice spots along one axis as a long-range orthorhombic superstructure is established on increasing the La content from $x = 0.5$ to $x = 0.6$. The direct evidence of vacancy ordering provided by the lattice images is the most striking observation reported in this paper.

Of the quenched samples, only the La-rich composition $x = 0.6$ showed superlattice formation when examined by XRD. The ordering apparent in the ED pattern of the quenched $x = 0.5$ composition (Fig. 5a) can therefore be assumed to occur only in the microstructure and not in the bulk structure. The superlattice reflections along the cubic [011] direction are only seen in the slow-cooled samples, thus demonstrating that the ordering is greater in these

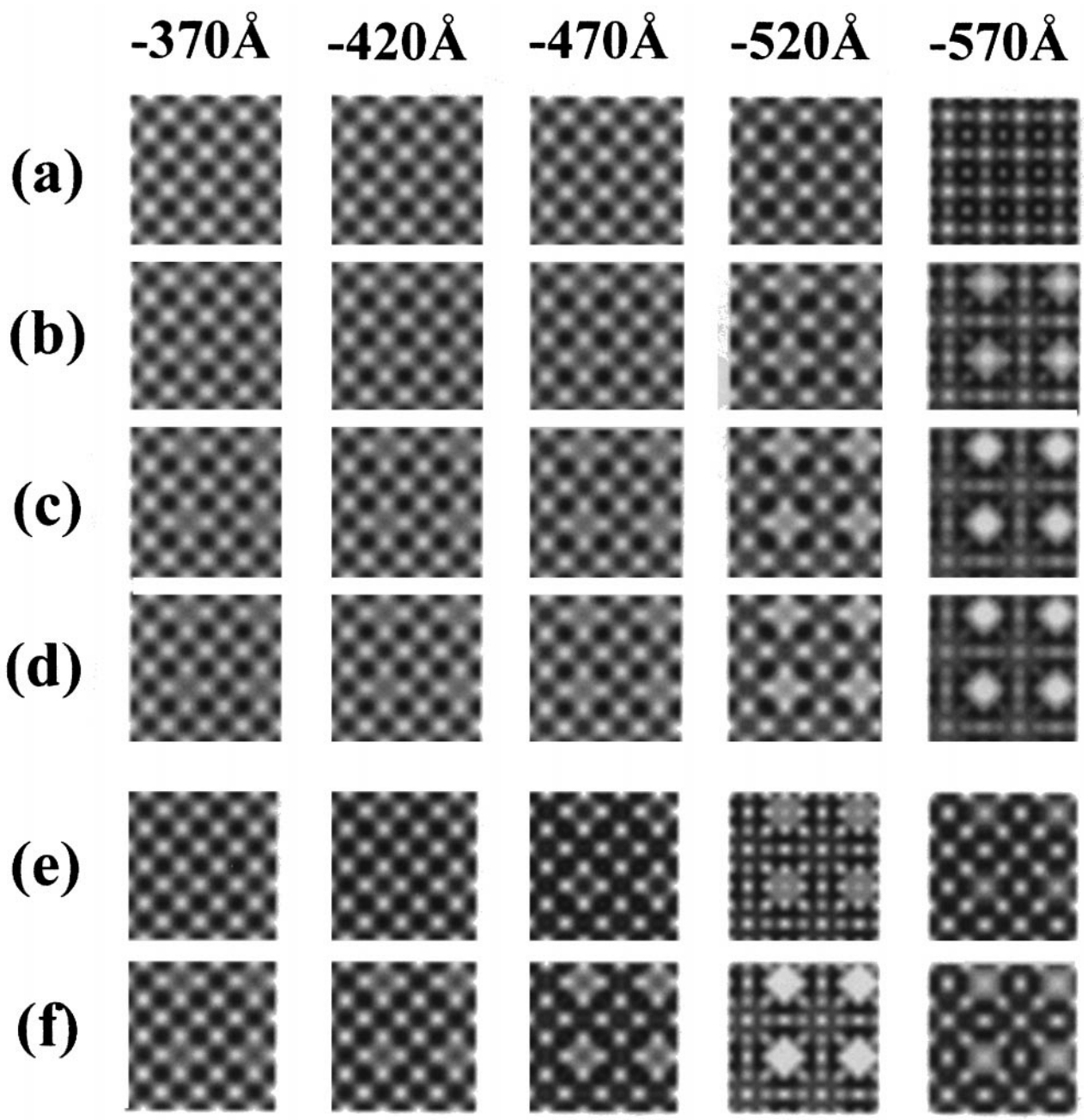

FIG. 8. Simulated [100] lattice images of a (4×4) perovskite supercell as a function of defocus: (a) 4 layers thick, no vacant A sites; (b) 4 layers thick, alternate A sites vacant in layer 1 only; (c) 4 layers thick, alternate A sites vacant in layers 1 and 2; (d) 4 layers thick, alternate A sites vacant in layers 1 and 3; (e) 8 layers thick, alternate A sites vacant in layers 1 and 5; (f) 8 layers thick, alternate A sites vacant in layers 1, 3, 5, and 7.

cases. There is a predominance of square vacancy groups in Fig. 6c but with some evidence for the development of ordered orthorhombic regions toward the top of the micrograph, the orthorhombic z axis running parallel to the 16-Å scale bar. The variation in the degree of vacancy ordering within one crystallite can be seen (Fig. 7) by comparing the diffraction patterns calculated by Fourier transforming regions A and B of the slow-cooled $x = 0.5$ sample; the superlattice spots generated by region A are much sharper than those generated from region B. The ordering is clearly not extensive enough in this particular crystallite for the orthorhombic region to dominate the ED pattern, even though the bulk sample showed orthorhombic symmetry in the X-ray experiment. The apparent variation between the local

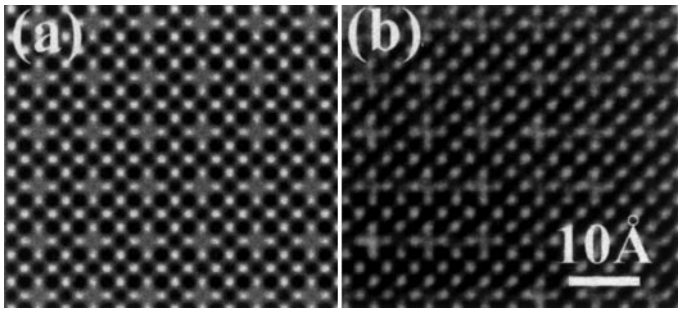

FIG. 9. (a) Image contrast calculated for a 30-Å-thick crystal with vacancies on alternating sites, as in Fig. 8f. (b) Real image of region *A′* in Fig. 7.

microstructure and the average crystal structure of the bulk necessitates caution in the interpretation of the XRD data collected on this system.

The manifestation of the superstructure in the XRD and ED patterns of $Sr_{1-3x/2}La_xTiO_3$ is similar to that reported previously (13) for the closely related $SrTiO_3$–$Nd_2Ti_2O_7$ system, thus suggesting that the model of cation-vacancy ordering described above might also be valid in that system.

REFERENCES

1. T. Y. Tien and F. A. Hummel, *Trans. British Ceram. Soc.* **66,** 233 (1967).
2. M. Abe and K. Uchino, *Mater. Res. Bull.* **9,** 147 (1974).
3. J. Bouwma, K. J. DeVries, and A. J. Burggraaf, *Phys. Status Solidi A* **35,** 281 (1976).
4. S. S. Shoup, T. J. Haverlock, and C. E. Bamberger,. *J. Am. Ceram. Soc.* **78,** 1261 (1995).
5. U. Balachandran and N. G. Eror, *J. Am. Ceram. Soc.* **64,** C75 (1981).
6. H. M. Rietveld, *J. Appl. Crystallogr.* **2,** 65 (1969).
7. A. C. Larson and R. B. von-Dreele, "General Structure Analysis System (GSAS)," Los Alamos National Laboratories, Report LAUR 86-748, 1990.
8. P. A. Stadelmann, *Ultramicroscopy* **21,** 131 (1987).
9. Digital Micrograph, Gatan Inc., copyright 1997.
10. R. Moos, T. Bischoff, W. Menesklou, and K. H. Härdtl, *J. Mater. Sci.* **32,** 4247 (1997).
11. M. J. MacEachern, H. Dabkowska, J. D. Garrett, G. Amov, W. Gong, G. Liu, and J. E. Greedan, *Mater. Chem.* **6,** 2092 (1994).
12. B. C. Tofield and W. R. Scott, *J. Solid State Chem.* **10,** 183 (1974).
13. J. Sloan and R. J. D. Tilley, *J. Solid State Chem.* **121,** 324 (1996).